High-resolution angle-resolved photoemission study of electronic structure and electron self-energy in palladium

Hirokazu Hayashi,[1] Kenya Shimada,[2,*] Jian Jiang,[2] Hideaki Iwasawa,[2] Yoshihiro Aiura,[3] Tamio Oguchi,[4]
Hirofumi Namatame,[2] and Masaki Taniguchi[1,2]

[1]*Graduate School of Science, Hiroshima University, Kagamiyama 1-3-1, Higashi-Hiroshima 739-8526, Japan*

[2]*Hiroshima Synchrotron Radiation Center, Hiroshima University, Kagamiyama 2-313, Higashi-Hiroshima 739-0046, Japan*

[3]*National Institute of Advanced Industrial Science and Technology, Tsukuba, Ibaraki 305-8568, Japan*

[4]*Institute of Scientific and Industrial Research, Osaka University, Osaka 567-0047, Japan*

In this study, we investigate the electronic structure and electron self-energy of palladium single crystals using polarization-dependent high-resolution angle-resolved photoemission spectroscopy. The observed Fermi surfaces and energy-band dispersions agree with those given by the band-structure calculation. A detailed comparison between the observed and theoretical band dispersions of the Σ_1 band forming the electronlike Fermi surface indicates an electron-electron coupling parameter of $\lambda_{ee} \sim 0.02$. Near the Fermi level, a kink structure in the energy-band dispersion exists at ~ -20 meV, in agreement with the Debye energy. The electron-phonon coupling parameter is estimated to be $\lambda_{ep} = 0.39 \pm 0.05$ at 8 K for the Σ_1 band, which is consistent with the theoretical values of $\lambda_{ep} = 0.35$–0.41. Furthermore, analyses of the self-energy indicate a possible contribution from the electron-paramagnon interaction in the energy range of $-50 \sim -150$ meV. The evaluated electron-paramagnon coupling parameter is $\lambda_{em} \sim 0.06$ for the Σ_1 band. We found that the magnitudes of λ_{ep} and λ_{em} depend on the Fermi surface points. The total effective mass enhancement factor is estimated to be $1 + \lambda_{ep} + \lambda_{ee} + \lambda_{em} \sim 1.5$ for the Σ_1 band, which is close to the values $m^*/m_b \sim 1.5$–1.7 given by the de Haas–van Alphen and electron specific-heat measurements.

I. INTRODUCTION

Palladium (Pd) has attracted interest because it is widely used as a catalyst (Ref. 1) and it can store high-density hydrogen (Ref. 2). Palladium is located below nickel (Ni), which is ferromagnetic, in the periodic table. Although Pd is a paramagnetic metal, it tends to be magnetic based on the Stoner condition because the density of states (DOS) at the Fermi level (E_F) is high.[3] A recent neutron scattering study reported a clear observation of paramagnons in Pd.[4]

To understand the physical properties of Pd, it is important to clarify the electronic states. The occupied electronic states of Pd have been examined by angle-resolved photoemission (ARPES) spectroscopy (Refs. 5–9) and unoccupied electronic states by angle-resolved inverse photoemission spectroscopy (Ref. 10) and two-photon photoemission spectroscopy (Ref. 11). The results from ARPES experiments on Pd(111) and Pd(110) showed good agreement with the calculated band dispersions, which indicates that electron correlation is not significant in Pd 4d bands.[5,8,9,12] In contrast, the ARPES results for Ni showed a significant narrowing of the 3d bands compared with the calculated ones due to electron correlation.[13]

At photon energies near the Pd 4p-4d photoabsorption, however, one should consider multielectron excitations to account for the energy distribution curves (EDCs) and the constant-initial-energy curve.[6] Hora and Scheffler performed elaborate one-step calculations for Pd(111) and showed that a direct transition model was effective if one took into account the damping effect in the final states using the phenomenological optical potential.[7]

Yagi *et al.* have reported surface-derived states at −0.3 eV that deviated from the calculated bulk-derived bands.[8] Kang

et al. indicated that there is a non-negligible discrepancy between the theoretical DOS and the angle-integrated photoemission spectra of polycrystalline Pd film, while experimental band dispersions of Pd(111) agreed well with the calculated ones.[9] The slab calculation indicated that the DOS near the surface is narrower than that in the bulk.[9] The discrepancy between the theoretical and experimental DOS should be attributed primarily to the electronic states derived near the surface.[9]

The experimental electronic specific heat (Refs. 14 and 15) is enhanced compared with the value given by the band-structure calculation (Ref. 16), which is mainly derived from the many-body interaction. The electron-phonon coupling parameter was calculated as $\lambda_{ep} = 0.35$ (Ref. 17), 0.377 (Ref. 18), 0.40 (Ref. 19), and 0.41 (Refs. 20 and 21). Furthermore, combining the de Haas–van Alphen measurements and the theoretical electron-phonon coupling parameter, the electron-electron coupling parameter was estimated to be $\lambda_{ee} = 0.07$–0.15.[22] However, the contributions from the electron-electron (including electron-paramagnon) and electron-phonon interactions to the effective mass enhancement have not been experimentally evaluated so far.

The recent development of high-resolution ARPES enables us to examine quasiparticle properties near E_F in detail.[13,23,24] We have reported a high-resolution ARPES study of Pd(110) with a photon energy of $h\nu = 29$ eV at a temperature of 10 K, which revealed a kink structure in the energy-band dispersion.[24] However, we measured ARPES only at $h\nu = 29$ eV away from the high-symmetry point and did not fully analyze the obtained real and imaginary parts of the self-energy. In this study, we have performed extensive polarization-dependent high-resolution ARPES experiments

on Pd(110) and Pd(001). We have quantitatively analyzed the ARPES spectral line shapes and evaluated the electron self-energy. We discuss the magnitudes of the electron-phonon, electron-electron, electron-paramagnon, and electron-defect interactions on the quasiparticles.

II. EXPERIMENT

Single crystals of Pd(110) and Pd(001) (99.999%) were cleaned *in situ* by repeated cycles of Ar^+ sputtering (800 V) and subsequent annealing at 950 K. The amount of impurities, such as C, O, and S, on the surface was less than the detection limit of Auger electron spectroscopy. Clear and sharp 1×1 LEED spots confirmed that the atoms were well ordered and that no contaminants existed on the sample surface. We also verified the absence of contamination by angle-integrated photoemission spectra over a wide binding-energy range taken at $h\nu = 350$ eV.

All of the experiments were performed on the linear-undulator beamline (BL-1) of a compact electron-storage ring (HiSOR) at Hiroshima University,[25] using an ARPES system that can be rotated around linearly polarized undulator radiation.[26,27] The vector potential (**A**) of the excitation light was switched between parallel (*p* polarization) and perpendicular (*s* polarization) to the plane spanned by the surface normal and photoelectron propagation vectors, as shown in Fig. 1(a). The high-resolution ARPES measurements were performed using the angular mode of the hemispherical electron-energy analyzer (R4000, VG-Scienta, Sweden). For the high-resolution ARPES measurements near E_F, the total energy resolution was set to $\Delta E = 10$ meV, and a momentum resolution of $\Delta k = 0.007$ Å^{-1} was set for an incident photon energy of $h\nu = 21$, 23, 25, or 29 eV. For the measurements on the Fermi surface and band dispersions over a wide energy

range, we set $\Delta E = 100$ meV and $\Delta k = 0.068$ Å^{-1} for the photon energy of $h\nu = 160$ eV.

The ARPES measurements were performed by tuning the incident photon energy and by rotating the polar axis of the sample parallel to the [100] and [1$\bar{1}$0] directions for the (001) and (110) surfaces, respectively (Fig. 1). The light incidence angle was 50° relative to the lens axis of the electron analyzer. Fermi-surface mapping was conducted by rotating the azimuthal angle.

To analyze the spectral shapes quantitatively and evaluate coupling parameters of many-body interactions, we should survey the measurement condition for the narrowest linewidth by changing geometry and incident photon energy.[36] We found that the Σ_1 band taken at a photon energy of $h\nu = 21$ eV and at a polar angle of 45.5° with respect to the sample normal has the narrowest linewidth and is most suitable for the line-shape analyses. Here, we assumed an inner potential of $V_0 = 12.38$ eV (Ref. 9).

The sample was mounted on a liquid-He-flow-type five-axis goniometer (*i*-GONIO LT, R-dec Co., Japan)[28] and was cooled to $T = 8$ K ($h\nu = 21$ eV) and 80 K ($h\nu = 160$ eV) during the ARPES measurements. The base pressure of the measurement chamber was less than 7×10^{-9} Pa.

III. BAND-STRUCTURE CALCULATION

We have performed the band-structure calculation within the local density approximation in the fully relativistic scheme (scalar relativity plus spin-orbit coupling) using the full-potential linearized augmented-plane-wave method implemented with the HiLAPW program package. Figures 1(b) and 1(c) show the calculated Fermi surface contours in the high-symmetry plane. Figure 2(a) shows the calculated Fermi surfaces near the Fermi-surface point for the Σ_1 band. Figures 2(b) and 2(c) respectively show the energy-band dispersions along the *k* points of the arc for $h\nu = 21$ eV in Fig. 2(a) and along the thick dashed line in Fig. 2(a) with k_x at the Fermi wave number. The dispersion relation in Figs. 2(b) and 2(c) is used for the evaluation of the real part of the self-energy and the quantitative analyses of the ARPES linewidth.
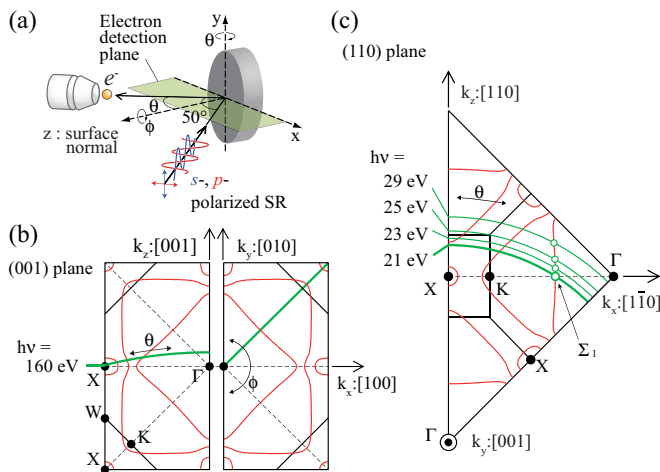

FIG. 1. (Color online) (a) A schematic view of the experimental geometry. The incident plane of the synchrotron radiation lies on the photoelectron detection plane. The electric field vector is on the detection plane in the *p*-polarization geometry, and it is perpendicular to the detection plane in the *s*-polarization geometry. (b) and (c) show the cross sections of the calculated Fermi surfaces and Brillouin zones of Pd(001) and Pd(110), respectively. The Σ_1 band is on the $\Gamma K X$ line. We measured the energy-band dispersions along the arcs shown in (b) and (c), which is dependent on the incident photon energy $h\nu$.
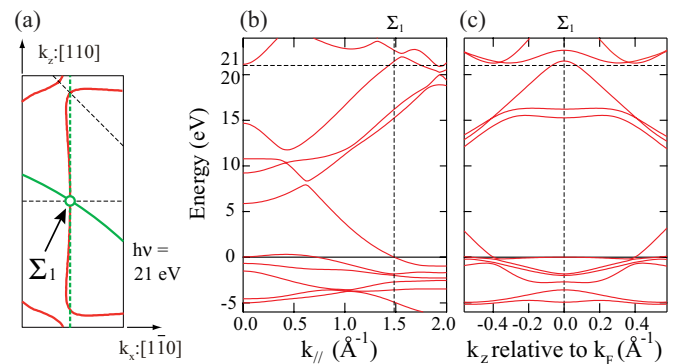

FIG. 2. (Color online) (a) Calculated Fermi surfaces and the Fermi-surface point for the Σ_1 band. (b) The calculated energy bands along the arc for $h\nu = 21$ eV in (a). (c) The calculated energy bands along the k_z direction (thick dashed line in (a) with k_x at the Fermi wave number).

IV. DIPOLE SELECTION RULE

The photoemission intensity (I) is proportional to the square of the dipole-transition matrix element $I \propto |\langle \phi_f^k | \mathbf{A} \cdot \mathbf{p} | \phi_i^k \rangle|^2$, where ϕ_i^k (ϕ_f^k) is the initial-state (final-state) electron wave function, and $\mathbf{p} = -i\hbar \nabla$ is a momentum operator.[29,30] Here, we employed the E1 approximation, and $\mathbf{A}$ is a constant vector parallel to the electric field vector $\mathbf{E}$, namely, $\mathbf{A} = (A_x, A_y, A_z) \parallel \mathbf{E}$. In this study, the photoelectron detection plane coincides with the mirror plane of the crystal; specifically, it lies in the xz plane [Fig. 1(a)]. We assumed that the final-state wave function ϕ_f^k should be free-electron-like and that ϕ_f^k should not change its sign under the symmetry operation $y \to -y$, even function with respect to the mirror plane.

In the p-polarization geometry, $\mathbf{A}$ is on the mirror plane, and the operator part $\mathbf{A} \cdot \mathbf{p} = -i\hbar(A_x \partial_x + A_z \partial_z)$ is even under the symmetry operation $y \to -y$. If the initial state is an odd function with y, namely, $\phi_i^k(x, -y, z) = -\phi_i^k(x, y, z)$, then the matrix element should be exactly zero because $\int_{-\infty}^{\infty} (\phi_f^k)^* [-i\hbar(A_x \partial_x + A_z \partial_z)] \phi_i^k dy = 0$. Therefore, the detectable initial states should be even with respect to the mirror plane. This selection rule is rigorous for the dipole transition in the bulk with a negligible spin-orbit interaction.[30]

For the s-polarization geometry, $\mathbf{A}$ is perpendicular to the mirror plane, giving $\mathbf{A} \cdot \mathbf{p} = -i\hbar A_y \partial_y$ an odd operator with respect to a symmetry operation of $y \to -y$. The detectable initial state, therefore, should be odd with respect to the mirror plane. Thus, we can selectively observe even or odd initial states with respect to the mirror plane by changing the polarization geometry.[29,30]

V. EMISSION-ANGLE DEPENDENCE OF THE LINEWIDTH BROADENING

The observed photoemission linewidth or the EDC width $\Gamma(\omega)$ can be described by the convolutions of the width in the initial state $\Gamma_i(\omega)$ and in the final state $\Gamma_f(\omega)$, $\Gamma = \Gamma_i \bigotimes \Gamma_f$.[31–33] The uncertainty in the wave vector (δk) of a Bloch function caused by interactions gives linewidths of $\Gamma_i = |\frac{\partial \varepsilon_i}{\partial k} \cdot \delta k|$ and $\Gamma_f = |\frac{\partial \varepsilon_f}{\partial k} \cdot \delta k|$, where $\frac{1}{\hbar} \frac{\partial \varepsilon_i}{\partial k} = v_i$ and $\frac{1}{\hbar} \frac{\partial \varepsilon_f}{\partial k} = v_f$ describe the group velocities of the initial and final states, respectively. The linewidth is expressed as

$$\Gamma(\theta) = \frac{\frac{\Gamma_i}{|v_{i\perp}|} + \frac{\Gamma_f}{|v_{f\perp}|}}{\left| \frac{1}{v_{i\perp}} \cdot \left(1 - \frac{m v_{i\parallel}}{\hbar k_\parallel} \sin^2\theta\right) - \frac{1}{v_{f\perp}} \cdot \left(1 - \frac{m v_{f\parallel}}{\hbar k_\parallel} \sin^2\theta\right) \right|},$$

(1)

where θ is the emission angle measured from the sample surface normal, $v_{i\perp}$ ($v_{f\perp}$) is the group velocity component perpendicular to the sample surface of the initial (final) state, and $v_{i\parallel}$ ($v_{f\parallel}$) is the group velocity component parallel to the surface of the initial (final) state.[31–33]

In the present analyses, we examine the spectral features near E_F and approximate the band dispersions in the initial and final states by linear functions. The initial-state band dispersion along the $k_\parallel$ (wave-number component parallel to the surface) direction may be written as $\omega = -\hbar v_{i\parallel}(k_\parallel - k_F)$, where k_F is the Fermi wave number. Based on the energy conservation law,

one may have $\frac{\hbar^2 k^2}{2m} = E_K^{\max} + \omega$, where $E_K^{\max}$ is the maximum kinetic energy. At a surface, the equation $\frac{1}{k} = \frac{\sin\theta}{k_\parallel}$ should also hold. Using these equations, the spectral width can be rewritten as a function of ω as

$$\Gamma(\omega) = \frac{\Gamma_0(\omega)}{\left| 1 - \zeta + \left(-1 + \zeta \frac{v_{f\parallel}}{v_{i\parallel}}\right) \frac{\hbar v_{i\parallel} k_F - \omega}{2(E_K^{\max} + \omega)} \right|},$$

(2)

where $\Gamma_0(\omega) = \Gamma_i(\omega) + |\zeta| \Gamma_f(\omega)$ and $\zeta = \frac{v_{i\perp}}{v_{f\perp}}$. We employ this equation to analyze the ARPES linewidth of Pd.

VI. RESULTS AND DISCUSSION

A. Fermi surfaces and band dispersions

Figures 3(a) and 3(b) show image plots of the observed Fermi surfaces in the ΓXWK plane taken at $h\nu = 160$ eV with the p-polarization geometry and s-polarization geometry, respectively. These images were obtained by integrating the spectral intensity near E_F. The calculated bulk-derived Fermi surfaces in the ΓXWK plane on the left side of Figs. 3(a) and 3(b) agree with the observed ones. Based on the calculation, an electronlike Fermi surface exists around the Γ point, and two holelike Fermi surfaces exist around the X point and along the X-W direction.[34]

These image plots show a significant polarization dependence of the photoemission intensity. In Fig. 3(a), the spectral intensity with the p-polarization geometry vanished at the Σ_2 band point. By contrast, the spectral intensity is strong with the s-polarization geometry [Fig. 3(b)]. These observations are consistent with the fact that the Σ_2 band crossing E_F along the Σ line is odd with respect to the mirror plane ($x = y$ plane).

Table I lists the basis functions along the Σ line and the symmetry under the reflection operation with respect to the $x = y$ mirror plane. The initial states with even and odd symmetry can be observed with the p- and s-polarization geometries, respectively.
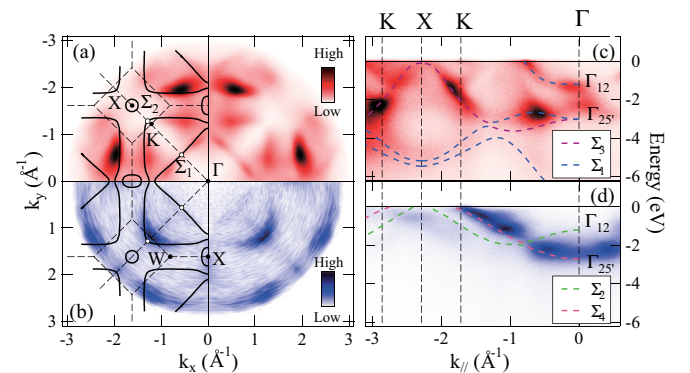

FIG. 3. (Color online) The observed Fermi surfaces of Pd(001) taken at $h\nu = 160$ eV with the p-polarization geometry (a) and the s-polarization geometry (b). The left-hand side of the image plots shows the calculated Fermi surfaces (solid lines) and the Brillouin zone boundary of the ΓKWX plane and the high-symmetry lines (broken lines). The ARPES image plots of Pd(001) are shown along the ΓKX direction with the p-polarization geometry (c) and the s-polarization geometry (d). The dashed curves in (c) and (d) show the calculated band dispersions.

TABLE I. The basis functions along the Σ line and their symmetries with respect to the mirror plane ($x = y$ plane).

Band	Σ_1	Σ_2	Σ_3	Σ_4
Basis function	1	$z(x-y)$	z	$x-y$
Symmetry	Even	Odd	Even	Odd

Figures 3(c) and 3(d) show image plots of the observed band dispersions along the Σ line. In the image plot with the *p*-polarization geometry [Fig. 3(c)], the energy band at -1.2 eV at $k_\parallel = 0$ Å^{-1} (Γ_{12}) disperses upward with decreasing $k_\parallel$ and crosses E_F at $k_F = -0.8$ Å^{-1}. The degenerated energy bands at -3 eV at $k_\parallel = 0$ Å^{-1} (Γ'_{25}) are split into the Σ_1 and Σ_3 bands. The observed Σ_3 band clearly disperses upward with decreasing $k_\parallel$ and is located in close proximity to E_F at the X point. However, in the image plot with the *s*-polarization geometry [Fig. 3(d)], the Σ_2 band located at -2.7 eV at $k_\parallel = 0$ Å^{-1} (Γ'_{25}) shows upward dispersion with decreasing $k_\parallel$ and crosses E_F at $k_F = -1.70$ Å^{-1}.

These observations agree with the calculated band dispersions and their symmetry properties and are consistent with previous ARPES studies[5–9] for Pd(111) and Pd(110) in that the observed band points agreed well with the theoretical ones.

B. Σ_1-band dispersion near E_F

Figures 4(a) and 4(c) show the ARPES intensity plot of the Σ_1 band taken at $h\nu = 21$ eV with the *p*-polarization geometry over a wide energy range and near E_F, respectively. The observed energy-band dispersion agrees with the calculated band dispersion along the arc in the k space, as shown in Fig. 1(c) for $h\nu = 21$ eV.

To analyze the spectral shape, we used a Voigt function on a linear background to fit the momentum distribution curves (MDCs) [Fig. 4(e)]. The Gaussian width was fixed to represent the momentum resolution of $\Delta k = 0.007$ Å^{-1}. We obtained the peak position [dots in Figs. 4(b) and 4(d)] and the Lorentzian width (δk) as functions of the energy (ω).

As shown in Figs. 4(b) and 4(d), the observed band dispersion in the wide energy range agrees with the theoretical dispersion. However, near E_F [Fig. 4(e)], a kink structure is recognizable in the band dispersion at $\omega \sim -20$ meV. Note that the bulk Debye energy $k_B\Theta_D = 23.6$ meV (Debye temperature: $\Theta_D = 274$ K) (Refs. 16 and 35) coincides with the energy scale of the kink. The kink at ~ -20 meV can be reasonably assumed to be derived from the electron-phonon interaction. Figure 4(f) shows EDCs (1,2,3) obtained from cuts along the white broken lines in Fig. 4(c). The EDC width becomes narrower as the peak approaches E_F.

C. Self-energy analyses

To evaluate the magnitudes of many-body interactions on the quasiparticles, we quantitatively analyze the ARPES line shapes in this section. The ARPES spectral features are given by the single-particle spectral function $A(k,\omega)$. In this study of a Pd metal, we have assumed that the many-body interactions are short ranged. Hence, the k dependence of the self-energy may be neglected, so $\Sigma(k,\omega) \sim \Sigma(\omega)$. In this case, the spectral
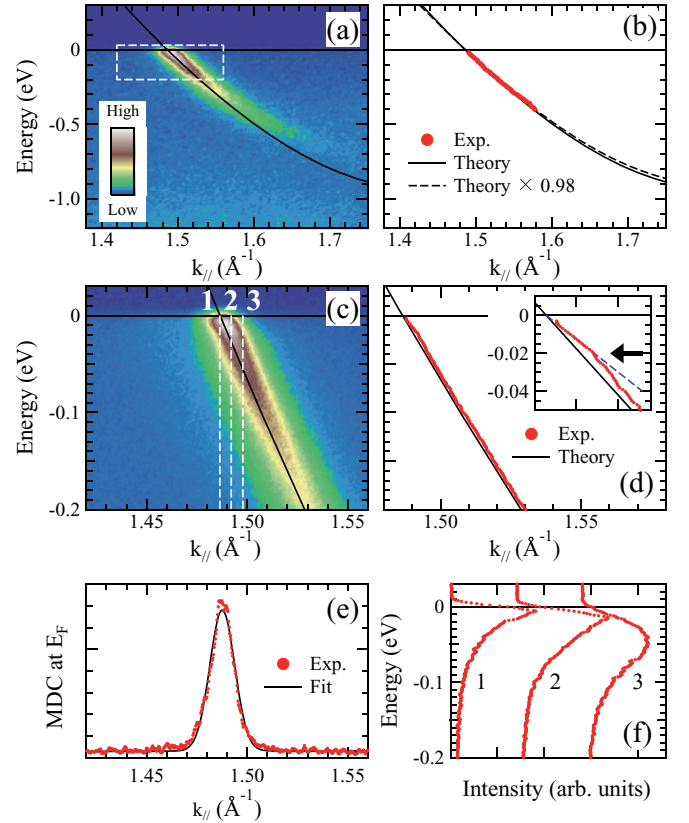

FIG. 4. (Color online) (a) ARPES image plot of Pd(110) taken at $h\nu = 21$ eV and at 8 K in the wide k and ω ranges. The solid line shows the calculated band dispersion. (b) The dots show the band positions determined by the MDC analyses. The solid line shows the calculated band dispersion. The dashed line is the calculated band dispersion multiplied by a factor of $1/(1 + \lambda_{ee}) = 0.98$. (c) A magnified ARPES image plot near E_F, which corresponds to the k and ω ranges indicated by the dashed area in (a). (d) The dots represent the band positions determined by the MDC analyses. A kink structure exists at ~ -20 meV. The inset shows magnified band dispersion near E_F. (e) The MDC at E_F fitted by a Voigt function on a linear background. (f) The EDCs along the dashed white lines 1, 2, and 3 in (c).

function is given by

$$A(k,\omega) = -\frac{1}{\pi} \frac{\mathrm{Im}\Sigma(\omega)}{\left[\omega - \omega_k^0 - \mathrm{Re}\Sigma(\omega)\right]^2 + \left[\mathrm{Im}\Sigma(\omega)\right]^2}, \quad (3)$$

where ω_k^0 represents the energy of the noninteracting band.[13,30,36,37]

In this study, we have assumed that the electron-scattering processes are independent and that the self-energy can be expressed as the sum of the self-energies derived from the electron-phonon interaction (Σ_{ep}), electron-electron interaction (Σ_{ee}), electron-paramagnon interaction (Σ_{em}), and electron-defect interaction (Σ_{ed}): $\Sigma = \Sigma_{ep} + \Sigma_{ee} + \Sigma_{em} + \Sigma_{ed}$.

The lifetime broadening of a quasiparticle is given by the imaginary part of the self-energy as $\Gamma_i = 2|\mathrm{Im}\Sigma| = \Gamma_{ep} + \Gamma_{ee} + \Gamma_{em} + \Gamma_{ed}$, where Γ_{ep}, Γ_{ee}, Γ_{em}, and Γ_{ed} denote lifetime broadening due to the electron-phonon, electron-electron,

electron-paramagnon, and electron-defect interactions, respectively. The $\Gamma_{ep} + \Gamma_{ee} + \Gamma_{em}$ term is energy dependent, whereas the Γ_{ed} term is energy independent.

The real part of the self-energy is obtained by the energy shift from the noninteracting band: $\mathrm{Re}\Sigma(\omega) = \omega - \omega_k^0$. Here we assume ω_k^0 is the band energy given by the band-structure calculation [Fig. 2(b)]. The dimensionless coupling parameter is evaluated by

$$\lambda = -\left.\frac{\partial\,\mathrm{Re}\Sigma(\omega)}{\partial\omega}\right|_{\omega=0}. \tag{4}$$

The real part of the self-energy can be written as $\mathrm{Re}\Sigma = \mathrm{Re}\Sigma_{ep} + \mathrm{Re}\Sigma_{ee} + \mathrm{Re}\Sigma_{em}$, and the coupling parameter is given by $\lambda = \lambda_{ep} + \lambda_{ee} + \lambda_{em}$. We should note that $\mathrm{Re}\Sigma_{ed}(\omega) = 0$ because the electron-defect scattering is assumed to be elastic $[\Gamma_{ed}(\omega) = \mathrm{const}]$.[38]

Because the self-energy is a causal function, $\mathrm{Re}\Sigma$ and $\mathrm{Im}\Sigma$ should be mutually related via the Kramers-Kronig transform

$$\mathrm{Re}\Sigma(\omega) = \frac{1}{\pi}P\int_{-\infty}^{+\infty}\frac{\mathrm{Im}\Sigma(\omega')}{\omega'-\omega}d\omega',$$

$$\mathrm{Im}\Sigma(\omega) = -\frac{1}{\pi}P\int_{-\infty}^{+\infty}\frac{\mathrm{Re}\Sigma(\omega')}{\omega'-\omega}d\omega'. \tag{5}$$

Based on Eqs. (1) and (2), the observed linewidth is not identical to Γ_i. Therefore, we calculated the initial-state lifetime broadening to be consistent with the observed $\mathrm{Re}\Sigma$ using the Kramers-Kronig transform [Eq. (5)].

1. Experimental real and imaginary parts of the self-energy

Figures 5(a) and 5(b) show the experimentally evaluated $\mathrm{Re}\Sigma_{\mathrm{exp}}(\omega)$ and $\mathrm{Im}\Sigma_{\mathrm{exp}}(\omega)$ at 8 K, respectively. The imaginary part of the self-energy $\mathrm{Im}\Sigma_{\mathrm{exp}}(\omega)$ was evaluated by the expression $\Gamma(\omega) = 2|\mathrm{Im}\Sigma_{\mathrm{exp}}(\omega)| = (\partial\varepsilon_k/\partial k)\cdot\delta k$. The real part of the self-energy $\mathrm{Re}\Sigma_{\mathrm{exp}}(\omega)$ was evaluated by the energy shift from the band energy given by the band-structure calculation.

2. Electron-phonon interaction

In Fig. 5(a), $\mathrm{Re}\Sigma_{\mathrm{exp}}$ has a peak at ~-20 meV, which gives a maximum energy shift of ~ 8 meV. In Fig. 5(b), on the other hand, the observed $2|\mathrm{Im}\Sigma_{\mathrm{exp}}|$ is reduced by ~ 20 meV above $\omega \sim -30$ meV.

To confirm that these features are derived from the electron-phonon interaction, we simulated $2|\mathrm{Im}\Sigma_{ep}|$ and $\mathrm{Re}\Sigma_{ep}$. The lifetime broadening due to the electron-phonon interaction is given by

$$\begin{aligned}\Gamma_{ep}(\omega,T) &= 2|\mathrm{Im}\Sigma_{ep}(\omega,T)|\\ &= 2\pi\int_0^\infty \alpha^2 F(\nu)[2n(\nu,T) + f(\nu+\omega,T)\\ &\quad + f(\nu-\omega,T)]d\nu,\end{aligned}$$

where $n(\nu,T)$ and $f(\nu,T)$ are the Bose-Einstein and Fermi-Dirac distribution functions, respectively.[13,37] We used the theoretical phonon DOS (Ref. 18) for $F(\omega)$ and assumed α is an energy-independent adjustable parameter.[13,36] Using the Kramers-Kronig transform [Eq. (5)], we calculated $\mathrm{Re}\Sigma_{ep}$ using theoretical $\mathrm{Im}\Sigma_{ep}$.
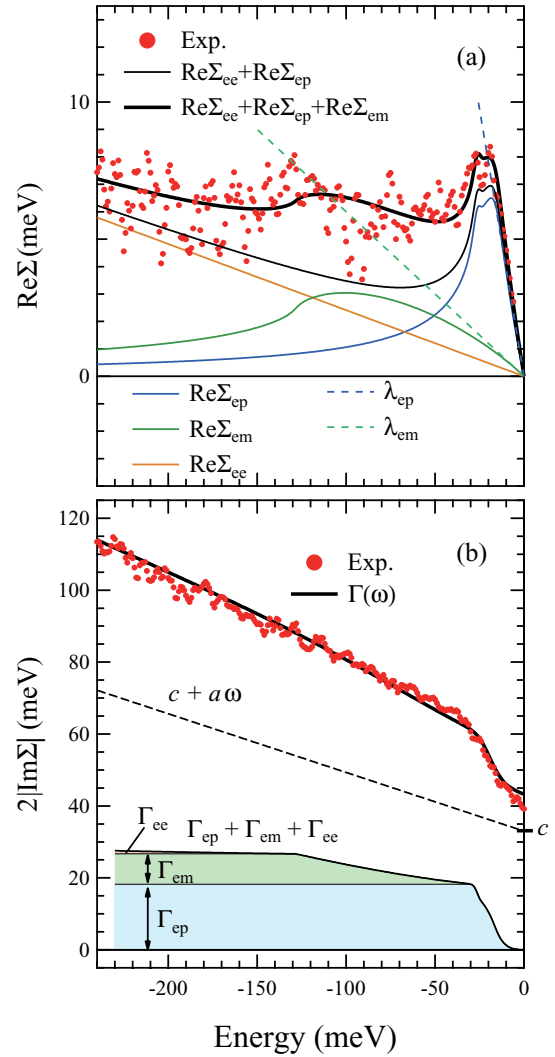

FIG. 5. (Color online) The evaluated self-energy for the Σ_1 band based on the ARPES results taken at $h\nu = 21$ eV at a temperature of 8 K. (a) The dots represent $\mathrm{Re}\Sigma_{\mathrm{exp}}$. The thin solid curves show the respective contributions from the electron-phonon ($\mathrm{Re}\Sigma_{ep}$), electron-paramagnon ($\mathrm{Re}\Sigma_{em}$), and electron-electron ($\mathrm{Re}\Sigma_{ee}$) interactions. The broken lines indicate the gradient at E_F of theoretical $\mathrm{Re}\Sigma_{ep}$ and $\mathrm{Re}\Sigma_{em}$. The thick solid line indicates $\mathrm{Re}\Sigma_{ee} + \mathrm{Re}\Sigma_{ep} + \mathrm{Re}\Sigma_{em}$. (b) The dots and thick line represent $2|\mathrm{Im}\Sigma_{\mathrm{exp}}|$ and $\Gamma(\omega)$, respectively. The dashed line indicates a contribution from $c + a\omega$ to $\Gamma_0(\omega)$. The thin curves at the bottom show the linewidths due to the electron-phonon (Γ_{ep}), electron-paramagnon (Γ_{em}), and electron-electron (Γ_{ee}) interactions.

As evident in Figs. 5(a) and 5(b), the energy dependencies of $\mathrm{Re}\Sigma_{\mathrm{exp}}$ and $2|\mathrm{Im}\Sigma_{\mathrm{exp}}|$ are explained well by the theoretical $\mathrm{Re}\Sigma_{ep}$ and $2|\mathrm{Im}\Sigma_{ep}|$ in the energy range of $\omega = 0 \sim -30$ meV. This result confirms that the energy dependence of the observed self-energy near E_F is mainly derived from the electron-phonon interaction.

We evaluated the coupling parameter λ_{ep} based on the gradient of the calculated $\mathrm{Re}\Sigma_{ep}$ [dashed line in Fig. 5(a)] and obtained $\lambda_{ep} = 0.39 \pm 0.05$. This value agrees with the theoretical coupling parameters $\lambda_{ep}^{\mathrm{th}} = 0.35$ (Ref. 17), 0.377 (Ref. 18), 0.40 (Ref. 19), and 0.41 (Refs. 20 and 21).

3. Electron-electron interaction

To simulate the self-energy due to the electron-electron interaction, we adopted a phenomenological model[26,36,39]

$$\mathrm{Im}\Sigma_{ee} = \frac{-\beta\xi^4\omega^2}{(\omega^2+\xi^2)^2}, \quad \mathrm{Re}\Sigma_{ee} = \frac{-\beta\xi^3\omega(\omega^2-\xi^2)}{2(\omega^2+\xi^2)^2},$$

where β and ξ are adjustable parameters. Note that these functions satisfy the general properties of Fermi-liquid theory near E_F, and $\mathrm{Re}\Sigma_{ee}$ and $\mathrm{Im}\Sigma_{ee}$ are exactly related via the Kramers-Kronig transform. In this analysis, we assumed $\xi \sim -3.7$ eV to be the onsite Coulomb interaction,[26,40] and $\beta = 0.013$ eV^{-1} was obtained through the fitting of $\mathrm{Re}\Sigma_{\mathrm{exp}}$.

Based on the fitting using this analytical function, the electron-electron coupling parameter was evaluated to be $\lambda_{ee} = -\beta\xi/2 = 0.024$. The calculated band dispersion multiplied by a factor of $1/(1+\lambda_{ee}) \sim 0.98$ was consistent with the observed band dispersion [Fig. 4(b)]. These analyses indicated that the magnitude of the electron-electron interaction is much smaller than that of the electron-phonon interaction.

4. Electron-paramagnon interaction

In Fig. 5(a), clear differences between $\mathrm{Re}\Sigma_{\mathrm{exp}}$ and $\mathrm{Re}\Sigma_{ep} + \mathrm{Re}\Sigma_{ee}$ are shown, particularly around the energy range $\omega = -50 \sim -150$ meV. We should note that this situation is similar for $\mathrm{Re}\Sigma$ evaluated for $h\nu = 23$, 25, and 29 eV (Fig. 6).

Considering that the energy scale $50 \sim 150$ meV is comparable with the paramagnons observed in the inelastic neutron scattering measurements (Ref. 4) and that it is larger than the Debye energy $\sim$24 meV, we assumed that a contribution from the electron-paramagnon interaction should exist.

To simulate the self-energy due to the electron-paramagnon interaction Σ_{em}, we calculated the linewidth under the assumption that $\alpha^2 F(\nu) \rightarrow \alpha^2\rho_m(\nu) = C\omega^{1/2}$ $(0 < \nu < \omega_c)$, where $\rho_m(\nu)$ is the paramagnon DOS, C is an adjustable constant, and ω_c is the cutoff energy of the paramagnon DOS.[35,41,42]

The thick solid line in Fig. 5(a) represents the sum of $\mathrm{Re}\Sigma_{ep} + \mathrm{Re}\Sigma_{ee} + \mathrm{Re}\Sigma_{em}$ that reproduces $\mathrm{Re}\Sigma_{\mathrm{exp}}$ for the entire energy range. The coupling parameter due to the electron-paramagnon interaction was evaluated to be $\lambda_{em} = 0.06 \pm 0.03$ [dashed line in Fig. 5(a)]. The observed gradient of $\mathrm{Re}\Sigma_{\mathrm{exp}}$ at E_F was best reproduced by the sum of $\lambda_{ep} + \lambda_{ee} + \lambda_{ep} \sim 0.47$.

By changing the incident photon energy $h\nu$, we evaluated $\mathrm{Re}\Sigma_{\mathrm{exp}} - \mathrm{Re}\Sigma_{ee}$ at different Fermi surface points (Fig. 6). One can see the hump structure corresponding to the cutoff energy (ω_c) of the paramagnon DOS and the magnitudes of $\mathrm{Re}\Sigma_{em}$ depend on the Fermi surface points. We decomposed $\mathrm{Re}\Sigma_{\mathrm{exp}} - \mathrm{Re}\Sigma_{ee}$ into contributions from $\mathrm{Re}\Sigma_{ep}$ and $\mathrm{Re}\Sigma_{em}$ and evaluated the coupling parameters λ_{ep} and λ_{em} (see dashed lines in Fig. 6). Figure 7 exhibits the $h\nu$ dependence of these coupling parameters. Although we need to examine more points up to the Δ point, we can see that the electron-phonon and electron-paramagnon coupling parameters depend on the Fermi-surface points. For further analyses, we need detailed theoretical consideration of the electron self-energy derived from the electron-paramagnon interaction.
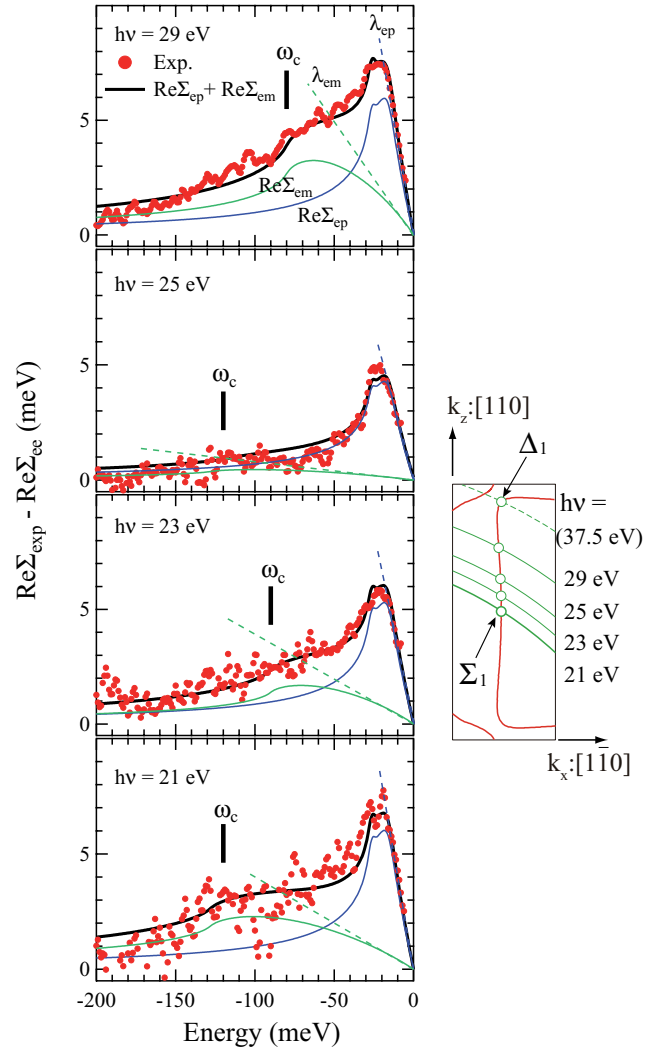

FIG. 6. (Color online) Incident photon energy dependence of $\mathrm{Re}\Sigma_{\mathrm{exp}} - \mathrm{Re}\Sigma_{ee}$. The thin curves indicate the contributions from $\mathrm{Re}\Sigma_{ep}$ and $\mathrm{Re}\Sigma_{em}$. The dashed lines indicate a gradient at E_F of theoretical $\mathrm{Re}\Sigma_{ep}$ and $\mathrm{Re}\Sigma_{em}$. ω_c indicates the cutoff energy of the paramagnon DOS. The figure on the right shows the Fermi-surface points measured at $h\nu = 21$, 23, 25, and 29 eV.

5. Final-state broadening and electron-defect interaction

The energy dependence of the initial-state linewidth broadening can be derived from $\Gamma_i(\omega) = \Gamma_{ep}(\omega) + \Gamma_{ee}(\omega) + \Gamma_{em}(\omega) + \Gamma_{ed}$, where Γ_{ed} is energy independent. The energy dependence of $\Gamma_i(\omega)$ can not explain the observed linewidth below $\omega \sim -50$ meV [Fig. 5(b)]. Therefore, we should consider the contribution from the final-state broadening (Γ_f) based on Eq. (2).

In the present analyses, we referred to the results from the band-structure calculation [Figs. 2(b) and 2(c)] and fixed ratios of the group velocities as $\frac{\hbar v_{f\parallel}}{\hbar v_{i\parallel}} = \frac{8.25\,\mathrm{eV\text{\AA}}}{4.86\,\mathrm{eV\text{\AA}}} = 1.7$ and $\zeta = \frac{v_{i\perp}}{v_{f\perp}} \propto \frac{m_f}{m_i} = 0.017$, where m_i (m_f) is the band mass for the initial (final) state. As the band dispersions along the k_z direction in Fig. 2(c) take the maximum near the Fermi wave number, we used the band mass for the evaluation of the ζ value. From the experimental data, we used $E_K^{\mathrm{max}} = 16.2$ eV,
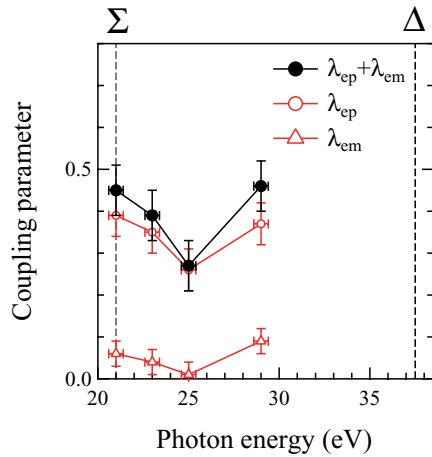
FIG. 7. (Color online) The incident photon energy dependence of λ_{ep}, λ_{em}, and $\lambda_{ep} + \lambda_{em}$. The Fermi-surface points are shown on the Σ and Δ lines at $h\nu = 21$ and 37.5 eV, respectively.

$k_F = 1.486$ Å^{-1}. Referring to the observed $2|\text{Im}\Sigma_{\text{exp}}(\omega)|$ and the calculated final-state energy-band dispersions in Figs. 2(b) and 2(c), we assumed that $\Gamma_f(\omega)$ is a regular function for the energy range we examined. Then, we employed the Taylor expansion of the final-state broadening expressed as $|\zeta|\Gamma_f(\omega) \sim \Gamma_f^0 + a\omega$ ($\omega < 0$), where Γ_f^0 and a are constants. The numerator of Eq. (2) can be written as $\Gamma_0(\omega) = \Gamma_i(\omega) + |\zeta|\Gamma_f(\omega) \sim \Gamma_{ep}(\omega) + \Gamma_{em}(\omega) + c + a\omega$, where $c \equiv \Gamma_{ed} + \Gamma_f^0$ is a constant.

The functional forms of $\Gamma_{ep}(\omega)$ and $\Gamma_{em}(\omega)$ were calculated from the Kramers-Kronig transform of $\text{Re}\Sigma_{ep}(\omega)$ and $\text{Re}\Sigma_{em}(\omega)$, respectively. We neglected the contribution from $\Gamma_{ee}(\omega)$ because it is substantially smaller than $\Gamma_{ep}(\omega) + \Gamma_{em}(\omega)$. We optimized c and a to give the best fit to the experimental linewidth broadening. In Fig. 5(b), the calculated $\Gamma(\omega)$ successfully reproduced the observed energy dependence of experimental $2|\text{Im}\Sigma_{\text{exp}}|$ below -50 meV. From the fit, we obtained $c = 0.033$ eV and $a = -0.16$ eV^{-1}. The upper limit of Γ_{ed} may therefore be evaluated by $\Gamma_{ed} < c = \Gamma_{ed} + \Gamma_f^0 = 33$ meV.

We should note that the term $a\omega$ in the final-state broadening is indispensable to fit the observed energy dependence of the lifetime broadening. Similar analyses (not shown here) of the ARPES results taken at different photon energies also indicated that we should account for this type of final-state broadening.

6. Effective mass enhancement factor

We have clarified the respective contributions of the many-body interactions to the effective mass enhancement in this study. The sum of the coupling parameters due to electron-electron and electron-paramagnon interactions is $\lambda_{ee} + \lambda_{em} \sim 0.08$, which is $\sim 21\%$ of the coupling parameter due to the electron-phonon interaction $\lambda_{ep} \sim 0.39$. Therefore, in the case of Pd, the electronic specific heat or effective mass enhancement is mainly derived from the electron-phonon interaction.

Here, we compare our results with those from de Haas–van Alphen measurements and specific-heat measurements. Joss

and Crabtree estimated many-body enhancements on the Fermi surface of Pd using the cyclotron effective masses using the Korringa-Kohn-Rostoker (KKR) band-structure calculation and theoretical electron-phonon coupling parameter.[22] For the electronlike Fermi surface, the total coupling parameter was evaluated to be $\lambda_{\text{tot}} = 0.49$, and by subtracting $\lambda_{ep} = 0.41$ (Ref. 21), they estimated the electron-electron contribution as $\lambda = \lambda_{\text{tot}} - \lambda_{ep} = 0.08$.[22] This evaluation is fully consistent with our results $\lambda_{ee} + \lambda_{em} \sim 0.08$ even though our evaluation was performed on the specific point of the electronlike Fermi surface. In this study, we revealed that the electron-electron contribution was mainly derived from the electron-paramagnon interaction.

On the other hand, the ratio between the experimental electronic specific heat γ^{exp} (Refs. 14 and 15) and the theoretical value γ^{th} given by the band-structure calculation (Ref. 16) is $\gamma^{\text{exp}}/\gamma^{\text{th}} = m^*/m_b = 1 + \bar{\lambda}_{\text{tot}} \sim 1.66$, where $\bar{\lambda}_{\text{tot}}$ is the total coupling parameter averaged over the Fermi surfaces. The electron effective mass enhancement factor evaluated in this study for the Σ_1 band, $1 + \lambda_{ep} + \lambda_{ee} + \lambda_{em} \sim 1.5$, was slightly smaller than the value given from the electronic specific-heat measurements. The deviation is most likely derived from the stronger-coupling parameters of the holelike Fermi surfaces as suggested by the de Haas–van Alphen measurements.[22] Detailed evaluations of the coupling parameters for the holelike Fermi surfaces are desirable in the future.

VII. CONCLUSION

We have performed polarization-dependent high-resolution ARPES on Pd to elucidate the electronic structures and the electron self-energy. The observed Fermi surfaces and energy-band dispersions were reproduced reasonably well by the band-structure calculation. Based on a detailed comparison between the observed and theoretical dispersions, the electron-electron coupling parameter was evaluated to be $\lambda_{ee} \sim 0.02$, for the Σ_1 band forming the electronlike Fermi surface. A kink structure due to the electron-phonon interaction existed at ~ -20 meV, in agreement with the Debye energy. The electron-phonon coupling parameter was evaluated to be $\lambda_{ep} = 0.39 \pm 0.05$ at 8 K for the Σ_1 band, which is consistent with the theoretical electron-phonon coupling parameters $\lambda_{ep} = 0.35$–0.41. More detailed analyses of the real part of self-energy suggested a possible contribution from the electron-paramagnon interaction in the energy range $-50 \sim -100$ meV. The electron-paramagnon coupling parameter was evaluated to be $\lambda_{em} \sim 0.06$ for the Σ_1 band. The magnitudes of λ_{ep} and λ_{em} depend on the Fermi-surface points. The effective mass enhancement factor was mainly derived from the electron-phonon interaction, and it was evaluated to be $1 + \lambda_{ep} + \lambda_{ee} + \lambda_{em} \sim 1.5$, which was close to the values $m^*/m_b \sim 1.5$–1.7 estimated from the de Haas–van Alphen and electronic specific-heat measurements.

ACKNOWLEDGMENTS

---

*Corresponding author: kshimada@hiroshima-u.ac.jp

[1] N. Miyaura and A. Suzuki, Chem. Rev. **95**, 2457 (1995), and references therein.

[2] F. D. Manchester, A. San-Martin, and J. M. Pitre, J. Phase Equilibria **15**, 62 (1994), and references therein.

[3] H. Chen, N. E. Brener, and J. Callaway, Phys. Rev. B **40**, 1443 (1989).

[4] R. Doubble, S. M. Hayden, Pengcheng Dai, H. A. Mook, J. R. Thompson, and C. D. Frost, Phys. Rev. Lett. **105**, 027207 (2010).

[5] N. Dahlbäck, P. O. Nilsson, and M. Pessa, Phys. Rev. B **19**, 5961 (1979).

[6] P. O. Nilsson, C. G. Larsson, and W. Eberhardt, Phys. Rev. B **24**, 1739 (1981).

[7] R. Hora and M. Scheffler, Phys. Rev. B **29**, 692 (1984).

[8] K. Yagi, K. Higashiyama, S. Yamazaki, H. Yanashima, H. Ohnuki, H. Fukutani, and H. Kato, Surf. Sci. **231**, 397 (1990).

[9] J.-S. Kang, D. W. Hwang, C. G. Olson, S. J. Youn, K.-C. Kang, and B. I. Min, Phys. Rev. B **56**, 10605 (1997).

[10] P. D. Johnson and N. V. Smith, Phys. Rev. Lett. **49**, 290 (1982).

[11] A. Schäfer, I. L. Shumay, M. Wiets, M. Weinelt, Th. Fauster, E. V. Chulkov, V. M. Silkin, and P. M. Echenique, Phys. Rev. B **61**, 13159 (2000).

[12] F. J. Himpsel and D. E. Eastman, Phys. Rev. B **18**, 5236 (1978).

[13] M. Higashiguchi, K. Shimada, K. Nishiura, X. Y. Cui, H. Namatame, and M. Taniguchi, Phys. Rev. B **72**, 214438 (2005), and references therein.

[14] C. Büscher, T. Auerswald, E. Scheer, A. Schröder, H. V. Löhneysen, and H. Claus, Phys. Rev. B **46**, 983 (1992).

[15] B. W. Veal and J. A. Rayne, Phys. Rev. **135**, A442 (1964).

[16] O. K. Andersen, Phys. Rev. B **2**, 883 (1970).

[17] S. Y. Savrasov and D. Y. Savrasov, Phys. Rev. B **54**, 16487 (1996).

[18] T. Takezawa, H. Nagara, and N. Suzuki, Phys. Rev. B **71**, 012515 (2005).

[19] I. Yu Sklyadneva, A. Leonardo, P. M. Echenique, S. V. Eremeev, and E. V. Chulkov, J. Phys.: Condens. Matter **18**, 7923 (2006).

[20] F. J. Pinski, P. B. Allen, and W. H. Butler, Phys. Rev. Lett. **41**, 431 (1978).

[21] F. J. Pinski and W. H. Butler, Phys. Rev. B **19**, 6010 (1979).

[22] W. Joss and G. W. Crabtree, Phys. Rev. B **30**, 5646 (1984).

[23] T. Valla, A. V. Fedorov, P. D. Johnson, and S. L. Hulbert, Phys. Rev. Lett. **83**, 2085 (1999).

[24] M. Higashiguchi, K. Shimada, Y. Miura, X. Y. Cui, N. Tobita, Y. Aiura, H. Namatame, and M. Taniguchi, Phys. B (Amsterdam) **383**, 148 (2006).

[25] K. Shimada, M. Arita, Y. Takeda, H. Fujino, K. Kobayashi, T. Narimura, H. Namatame, and M. Taniguchi, Surf. Rev. Lett. **9**, 529 (2002).

[26] H. Iwasawa, Y. Yoshida, I. Hase, K. Shimada, H. Namatame, M. Taniguchi, and Y. Aiura, Phys. Rev. Lett. **109**, 066404 (2012).

[27] K. Fukutani, H. Hayashi, I. N. Yakovkin, T. R. Paudel, T. Habuchi, D. Hirayama, J. Jiang, H. Iwasawa, K. Shimada, N. Wu, Evgeny Y. Tsymbal, Ya. B. Losovyj, and P. A. Dowben, Phys. Rev. B **85**, 155435 (2012).

[28] Y. Aiura, H. Bando, T. Miyamoto, A. Chiba, R. Kitagawa, S. Maruyama, and Y. Nishihara, Rev. Sci. Instrum. **74**, 3177 (2003).

[29] A. Damascelli, Z. Hussain, and Z.-X. Shen, Rev. Mod. Phys. **75**, 473 (2003).

[30] S. Hüfner, in *Photoelectron Spectroscopy Principles and Applications*, 3rd ed. (Springer, Berlin, 2003).

[31] J. A. Knapp, F. J. Himpsel, and D. E. Eastman, Phys. Rev. B **19**, 4952 (1979).

[32] N. V. Smith, P. Thiry, and Y. Petroff, Phys. Rev. B **47**, 15476 (1993).

[33] T.-C. Chiang, Chem. Phys. **251**, 133 (2000).

[34] F. M. Mueller, A. J. Freeman, J. O. Dimmock, and A. M. Furdyna, Phys. Rev. B **1**, 4617 (1970).

[35] C. Kittel, in *Introduction to Solid State Physics*, 6th ed. (Wiley, New York, 1986).

[36] X. Y. Cui, K. Shimada, Y. Sakisaka, H. Kato, M. Hoesch, T. Oguchi, Y. Aiura, H. Namatame, and M. Taniguchi, Phys. Rev. B **82**, 195132 (2010).

[37] J. Jiang, K. Shimada, H. Hayashi, H. Iwasawa, Y. Aiura, H. Namatame, and M. Taniguchi, Phys. Rev. B **84**, 155124 (2011).

[38] S. Doniach and E. H. Sondheimer, in *Green's Functions for Solid State Physicists* (Addison-Wesley, Redwood City, 1974).

[39] M. Arita, K. Shimada, Y. Takeda, M. Nakatake, H. Namatame, M. Taniguchi, H. Negishi, T. Oguchi, T. Saitoh, A. Fujimori, and T. Kanomata, Phys. Rev. B **77**, 205117 (2008).

[40] E. Şaşıoğlu, C. Friedrich, and S. Blügel, Phys. Rev. B **83**, 121101 (2011).

[41] J. Schäfer, D. Schrupp, Eli Rotenberg, K. Rossnagel, H. Koh, P. Blaha, and R. Claessen, Phys. Rev. Lett. **92**, 097205 (2004).

[42] A. Hofmann, X. Y. Cui, J. Schäfer, S. Meyer, P. Höpfner, C. Blumenstein, M. Paul, L. Patthey, E. Rotenberg, J. Bünemann, F. Gebhard, T. Ohm, W. Weber, and R. Claessen, Phys. Rev. Lett. **102**, 187204 (2009).